Optical Materials 144 (2023) 114306

Contents lists available at ScienceDirect

Optical Materials

journal homepage: www.elsevier.com/locate/optmat

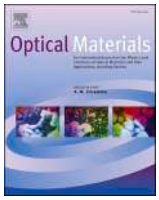

Research Article

Schottky junction based solar cell behavior of trichome hierarchical SnO_2 nano-structures

G. Mallik [a], A. Kabiraj [a], P.P. Dash [a], P. Kumari [a], Utkalika P. Sahoo [b], P.K. Sahoo [b], S. Rath [a,*]

[a] Nano-Structure and Soft-Matter Physics Laboratory, School of Basic Sciences, Indian Institute of Technology Bhubaneswar, Jatni, 752050, Odisha, India
[b] School of Physical Sciences, National Institute of Science Education & Research (NISER) Bhubaneswar, an OCC of Homi Bhabha National Institute, Jatni, 752050, Odisha, India

ARTICLE INFO

Keywords:
Tin dioxide (SnO_2)
Trichome nano-flowers
Hierarchical nano-structures
Optical properties
Schottky junction
Solar cell

ABSTRACT

Hydrothermally grown SnO_2 hierarchical trichome nano-flowers (T-NFLs) have been examined for their device performance compared to nano-flakes (NFs), in part to meet the growing need for metal-oxide based solar cells. The structural analyses reveal superior lattice strain and free energy in the tetragonal phase of the T-NFLs over NFs. The band gap widening and oxygen defect-dominated luminescence in the visible range are observed from photoluminescence measurements. Compared to NFs, the Schottky current-voltage characteristics of the T-NFLs show improved Schottky barrier height (0.82 eV) with an ideality factor of 3.52 under dark and better solar cell properties with a conversion efficiency of 1.78 ± 0.03% under 1 sun illumination. The observed high open-circuit voltage of 1.56 V resulted from the decrement rate of carrier recombination, making the transparent metal oxide nano-material SnO_2 T-NFLs suitable for solar cells and fast electronic applications.

1. Introduction

Metal-oxide (MO) nano-structures with size hierarchical properties are promising for nano-devices applications [1–4]. In the presence of a nano-dimensional MO interlayer, the Schottky barrier diode (SBD) shows an advantage over device performance by reducing the "barrier height effect" [5–7]. As observed by A. Baltakesmez et al., the zinc oxide (ZnO) interlayer makes the SBD tolerant in a radiation environment [8]. The graphene-oxide interlayer facilitates the device with an enhanced resistive switching effect [9], barrier height modulation [10], and overcomes the contact limitations [11], etc. Among the MO, Tin dioxide (SnO_2) is a well-known transparent conducting oxide (TCO) material [12,13] with co-existing metallic–semiconducting [14] behavior due to the flexible and degenerate band structures [15,16]. As an interface layer, the TCO stabilizes the SBD by enhancing barrier characteristics [9], prevents cross-contamination between active layers [17], and eases the transmission of electrical current and light flow through the devices [18]. The SnO_2 nano-material with various physical shapes, *viz.*, nano-rods, nano-sheets, nano-belts, nano-flowers, and nano-flakes, exhibit emerging field-emission properties, active electron transport layer (ETL), high-temperature photoconductivity, super-capacitor, and photo-catalytic behaviors, respectively [19–24] due to the quantum confinement effect. Therefore, the size hierarchical SnO_2 nanostructures are significant for technological implications. In addition, unlike p-n junction-based solar cells, SBD-based solar cells have reduced manufacturing complexity [11], improved radiation resistance [8], lower dark current [25], low forward voltage [7], and minimal loss caused by carrier recombination [26]. Therefore, the TCO-based SBD cells are appropriate for light harvesting across a wide range of wavelengths, enabling greater power conversion efficiency. At the same time, the crystalline structures of the MO influence charge transport [6], which ultimately determines the efficacy of the devices. Hence, the comprehension of the size-induced enhanced electrical response of SnO_2 nano-structures under photoexcitation is inevitable to establish SnO_2--based electronic devices.

This report describes (i) the growth of shape-hierarchical SnO_2 nano-structures (nano-flakes to trichome nano-flowers) through hydrothermal technique followed by structural characterization and property evaluation; (ii) intriguing transitions dominated luminescence in the visible range are revealed by optical measurements; and (iii) the shape-hierarchical SBD current-voltage characteristics have been investigated to explore the TCO based solar cells.

* Corresponding author.
E-mail address: srath@iitbbs.ac.in (S. Rath).

https://doi.org/10.1016/j.optmat.2023.114306
Received 6 June 2023; Received in revised form 21 August 2023; Accepted 25 August 2023
Available online 6 September 2023
0925-3467/© 2023 Elsevier B.V. All rights reserved.

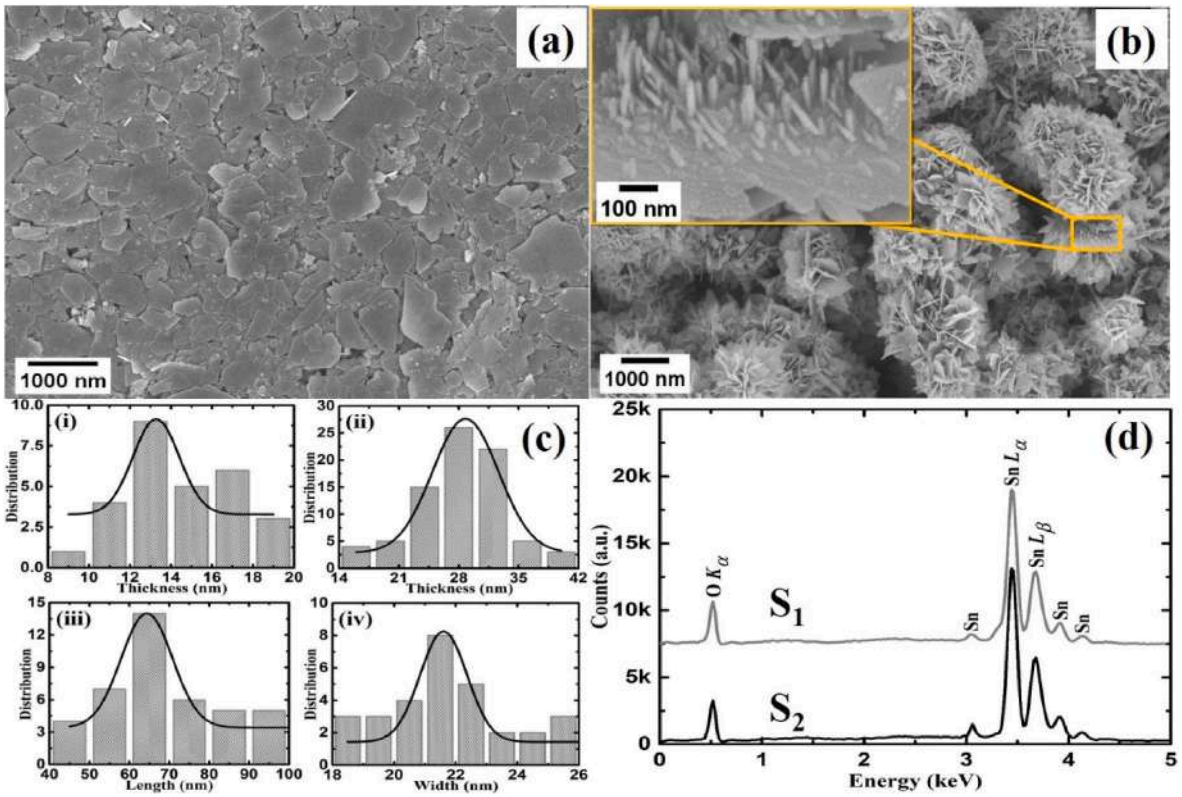

Fig. 1. FESEM micrographs of S_1 (a), S_2 (b) with the inset showing the growth of trichomes on the petals of the nano-flower structures. The thickness distribution histograms with Gaussian fittings (black solid curves) of S_1 (c) (i), S_2 (c) (ii), the length (c) (iii) and width (c) (iv) distributions with Gaussian fittings (black solid curves) of the trichomes. The EDS spectra of (d) S_1 (grey solid curve) and S_2 (black solid curve).

2. Experimental

The synthesis of size-hierarchical SnO_2 nano-materials is based on the alkali ion activated hydrothermal growth. The typical synthesis protocol consists of the following steps: (1) 0.25 M homogeneous $SnCl_2.2H_2O$ solution was taken in a 200 ml reagent bottle and heated at 393 K; and (2) 0.4 M KOH or 0.4 M NaOH solution was added dropwise to the above solution under vigorous stirring conditions during heating. (3) The resultant precursors were transferred to a 100 ml Teflon autoclave and heated at 453 K for 15 h, followed by natural cooling to room temperature (300 K). Two optimized samples, S_1 and S_2, were prepared using KOH and NaOH as alkali-ion stimulated reducing growth agents, respectively. Then, the final solution was cleaned with double-distilled deionized water and ethanol using a centrifuge. The precipitate was dried in a vacuum for 24 h, yielding the sandy-brown-colored SnO_2 nano-structure powders.

The structural and compositional behavior of the SnO_2 nano-structured samples were analyzed using Merlin Compact (Gemini-I electron column), Carl Zeiss, Germany, field emission scanning electron microscope (FESEM), and Oxford Instrument, energy dispersive x-ray spectroscope (EDS), respectively. To carry out the FESEM and EDS experiments, the water-dispersed samples were spin coated on cleaned silicon wafers. The x-ray diffractometer (XRD), Bruker D8 Advance diffractometer (Cu K_α, $\lambda = 1.5418$ Å [27]), operating at 40 kV and 40 mA, was used to investigate the crystal structures of the samples. The reproducibility of the growth process has been confirmed from FESEM, EDS, and XRD studies of several batches of samples. The Raman instrument, LabRam HR Raman instrument coupled with a CCD detector having 0.52 cm^{-1} spectral resolution, was utilized for the collection of Raman signals. The wavelength of 532 nm with power 30 mW from the He-Cd laser source was used as the Raman excitation line. Bruker α Alpha-T FTIR instrument was utilized to record the FTIR absorption spectra of the samples. The photoluminescence (PL) analysis has been carried out using Agilent Cary Eclipse Fluorescence Spectrophotometer. The Shimadzu UV-1800 Spectrophotometer was used to study the spectral absorption characteristics of the samples.

The electrical properties of the samples were characterized by constructing four junction devices: Au/S_1 (D_1), Au/S_2 (D_2), (Indium Tin Oxide) ITO/S_1 (D_3), and ITO/S_2 (D_4). To construct D_1 and D_2, metallic gold (Au) was sputter coated on a cleaned silicon dioxide (SiO_2) substrate using Quorum SC7620 sputter coating unit, followed by spin coating of the samples (S_1 or S_2). Similarly, the devices D_3 and D_4 were prepared on commercially available ITO substrates (thickness 200 nm), keeping other parameters constant. Here, the samples were spin coated at a rpm (rotations per minute) of 1200 for a duration of 3 min. Finally, using masking technique, silver (Ag) finger electrodes of thickness 200 nm and a total area of 0.03 cm^2 were sputter coated on the devices having total area 0.722 cm^2. The use of finger electrodes facilitates the transmission of light through the TOC for photovoltaic effects in place and avoids the impact of heterogeneity in sample distribution over the active layers. The transport properties of the devices D_1, D_2, D_3, and D_4 were analyzed using ScienceTech AAA Solar Simulator coupled with Keithley 2450 source meter. The devices were illuminated using a xenon lamp source in the presence of a 1.5 a.m. (air mass) filter. The reproducibility of SBD device behavior has been verified over a series of 10 samples from each batch.

3. Results and discussion

Fig. 1(a) and (b) are the FESEM micrographs of samples S_1 and S_2 respectively. From detailed analysis, it has been observed that sample S_1 exhibits nano-flake (NFs) structures, while S_2 exhibits nano-flower (NFLs) structures. At the same time, the inset of Fig. 1(b) reveals the growth of nano-rods on the surface of the petals of nano-flowers. These

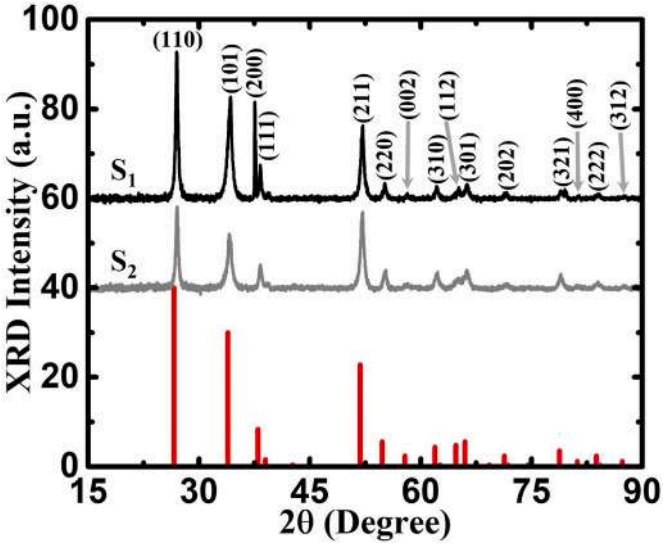

Fig. 2. XRD patterns of S_1 (black solid curve) and S_2 (grey solid curve), with the red colored bar plot indicating the peak positions and relative intensities of the standard JCPDS # 00-041-1445 data file.

studies yielded interesting nano-trichomes (i.e., upright nano-rods grown on the petal like structure) hierarchical nano-flower (T-NFLs) growth of S_2 in contrast to the nano-flake structure of sample S_1. From the size distribution analysis as shown in Fig. 1(c–(i) & (ii)), the mean thickness of nano-flakes and the mean petal thickness of nano-flowers were found to be 13.28 nm and 28.79 nm respectively. The average size of trichomes is estimated to be 64.38 nm (Fig. 1(c–(iii))) having width of 21.61 nm (Fig. 1(c–(iv))). The growth mechanism of trichomes hierarchical nano-flowers can be understood as follows. According to K. Sato et al. [28] and M. Guan et al. [29], the alkali-ion stimulated dissolution–precipitation reaction followed by in-situ crystallization [30] facilitates one-dimensional and two-dimensional growth. Further, it has been observed that by controlling the strength of interaction (e.g., the chemical reactivity of Na^+ ions (ionic radius ~ 0.19 nm) is greater than K^+ ions (ionic radius ~ 0.22 nm)) [31] and the concentration of alkali medium [29], a competitive reaction between dissolution–precipitation can be achieved, which facilitates for nano-flakes and nano-rods growth. Interestingly, the oxygen vacancy ridden crystallographic anisotropy present in the structure of the samples imposes additional hydrophobic-hydrophobic and hydrophilic-hydrophilic interactions that trigger a new dimensional growth process [28]. The chemical reactions involved in our synthesis protocol of samples S_1 and S_2 can be written as:

$$SnCl_2.2H_2O + 2KOH \rightarrow Sn(OH)_2 + 2KCl + 2H_2O$$

$$Sn(OH)_2 + 2KOH \rightarrow K_2SnO_3 + H_2O + H_2$$

$$K_2SnO_3 + H_2O \rightarrow SnO_2 + 2KOH$$

and

$$SnCl_2.2H_2O + 2NaOH \rightarrow Sn(OH)_2 + 2NaCl + 2H_2O$$

$$Sn(OH)_2 + 2NaOH \rightarrow Na_2SnO_3 + H_2O + H_2$$

$$Na_2SnO_3 + H_2O \rightarrow SnO_2 + 2NaOH$$

Here, the intermediate compounds potassium stannate (K_2SnO_3) and sodium stannate (Na_2SnO_3) are responsible for the typical growth of samples S_1 and S_2 due to the following interactions. The hydrophilic K_2SnO_3 is readily soluble in polar solvents, whereas the solubility of

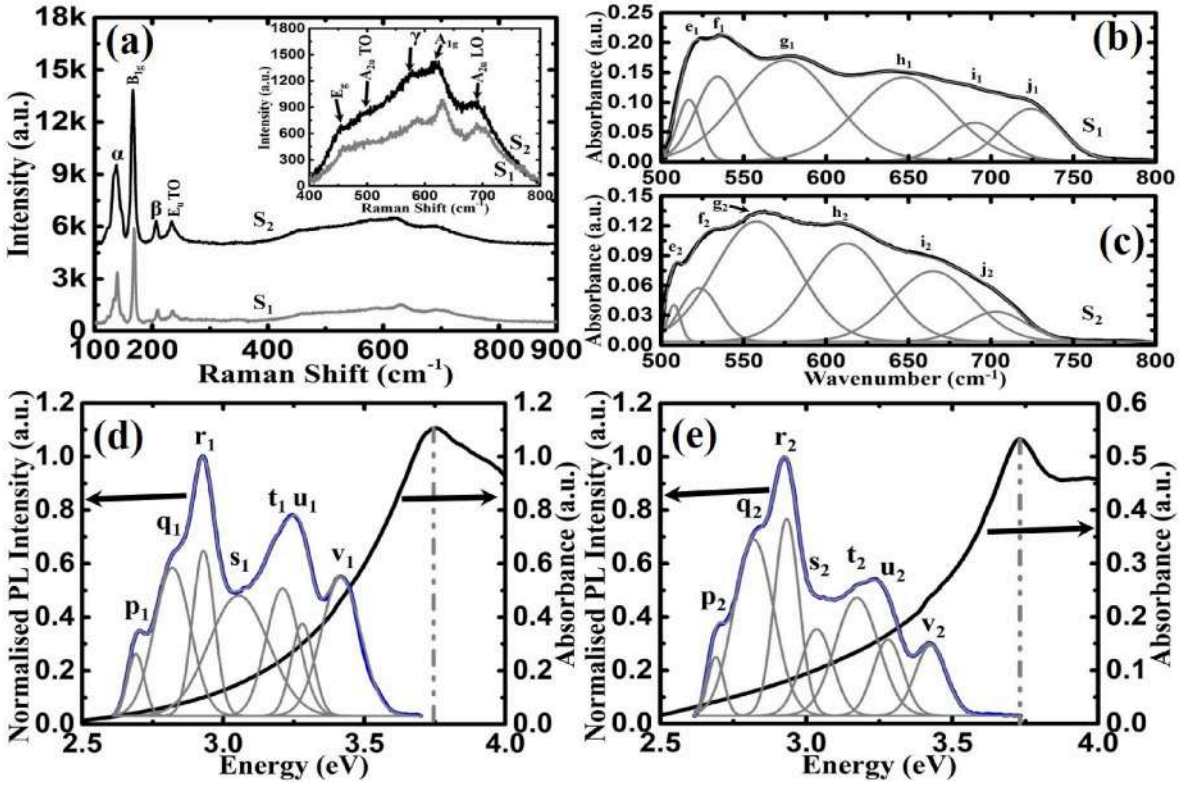

Fig. 3. Raman spectra (a) of S_1 (grey solid curve) and S_2 (black solid curve), with the insets depicting the magnified clear peak patterns of S_1 (grey solid curve) and S_2 (black solid curve) for the range 400 cm^{-1} to 800 cm^{-1}. The FTIR absorption spectra (black solid curve) with deconvoluted Gaussian peaks (grey solid curves) of S_1 (b) and S_2 (c). The PL emission spectra (blue solid curve) with deconvoluted Gaussian peaks (grey solid curves) and UV–vis absorption spectra (black solid curve) of S_1 (d) and S_2 (e).

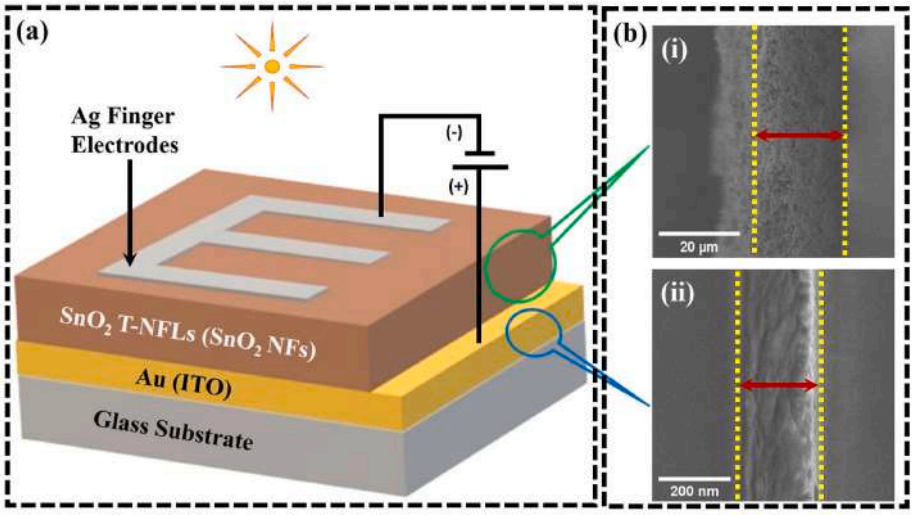

Fig. 4. (a) Schematic diagram of the fabricated devices under illumination showing the layer thicknesses. (b) The FESEM micrographs of cleaved devices indicating the thickness of (i) semiconductor and (ii) metal layers as 20 μm and 200 nm respectively.

Na_2SnO_3 is very poor in polar solvents, indicating hydrophobic nature. The hydrophobic-hydrophobic and hydrophilic-hydrophilic interactions may have confined crystal growth in one direction and formed trichomes on the petals of the nano-flowers. However, more work is required to understand the growth dynamics. The chemical composition versus energy plots of the samples S_1 and S_2 under the EDS are shown in Fig. 1(d). Detailed analysis estimates the atomic ratio of Sn:O as 1:2 for S_1 and 1:2.5 for S_2. The excess oxygen content of S_2 may have resulted from the absorption of atmospheric oxygen onto the surface of the complex hierarchical structure of T-NFLs. The crystal structures of the samples were investigated using XRD, and the diffraction patterns are shown in Fig. 2. The crystallographic planes are labelled and compared with JCPDS file # 00-041-1445. The x-ray diffraction lines are attributed to the tetragonal rutile structure [32] of the samples. From the prominent crystallographic plan (110), the lattice constants, c/a ratio, and unit cell volumes have been calculated and are summarized in Table SI1 (see SI). Notably, the lattice parameters (a, b, and unit cell volume) decrease in the order bulk > S_2 > S_1. This may be due to oxygen vacancies (OVs) mediated local lattice disorders [33]. Further, the diffraction peak positions and line widths of the samples S_1 and S_2 are observed to be shifted and broadened, indicating the presence of the size effect and vacancy dominated tensile stress and compressive stress in the samples [34,35]. Using the Debye-Scherrer Method (DSM), Williamson-Hall Method (WHM), and Size Strain Plot Method (SSPM) [36,37], the crystallite size, stress, strain, and surface free energy of the samples were estimated and listed in Table SI2 (see SI). From SSPM, it has been observed that the lattice strain and free energy of sample S_1 are greater than S_2. This may be due to the strong size confinement [38] in the NFs as compared to T-NFLs.

In order to understand the quantum confinement effect on the vibration modes, the samples were investigated using Raman spectroscopy and FTIR measurements. The results are shown in Fig. 3 (a, & b-c). As observed from Fig. 3 (a), the Raman peaks appearing at 168.443 cm^{-1}, 461.449 cm^{-1}, and 632.173 cm^{-1} refer to the B_{1g}, E_g, and A_{1g} Raman modes of S_1 respectively, indicating different degrees of stretching modes of Sn-O bonds [39]. Similar stretching modes are also observed in sample S_2 at 166.385 cm^{-1}, 448.455 cm^{-1}, and 623.639 cm^{-1}. The blue shift of Raman Peaks in S_1 compared to S_2 is possibly due to the presence of excess structural strain [40] (as obtained from SSPM) and/or a low concentration of defects [41] in S_1. Again, as shown in the inset of Fig. 3 (a), the infra-red (IR) active Raman peaks, E_u TO (Transverse Optical), A_{2u} TO, and A_{2u} LO (Longitudinal Optical), appeared at 234.452 cm^{-1}, 523.276 cm^{-1}, 690.609 cm^{-1} for S_1 and 233.452 cm^{-1}, 506.021 cm^{-1}, 679.204 cm^{-1} for S_2 respectively. The appearance of the IR-active modes may be due to the structural modifications induced by the size confinement effect [42] and the presence of disorders like oxygen vacancies (OVs) in the material [43] and lattice strain [44]. Apart from the above six peaks, additional peaks α, β and γ are observed at 139.573 cm^{-1}, 209.469 cm^{-1}, 594.030 cm^{-1} for S_1 and 138.022 cm^{-1}, 166.385 cm^{-1}, 584.016 cm^{-1} for S_2 respectively. The origin of peak α, may be due to the corner zone mode arising mainly from the wrinkle effect [45]. Similarly, the appearance of peaks, β and γ are due to the presence of SnO_x type materials with variable oxidation states of Sn [46] and defects in the structures, mainly oxygen vacancies (OVs) [45] respectively. In order to trace the IR vibrations, the experimental FTIR data were deconvoluted using the Gaussian function and plotted as Fig. 3(b and c). The low energy vibrational bands mainly correspond to O-Sn-O or Sn-O-Sn vibrational stretching (lattice vibrations) [47]. The peaks e_1 (516.784 cm^{-1}) and e_2 (507.714 cm^{-1}) correspond to the terminal oxygen vibrations [48] arising from the stretching of Sn-O bonds [49]. The quantum confinement induced characteristic FTIR peaks g_1 and g_2 have been observed at 575.332 cm^{-1} and 557.823 cm^{-1} respectively [50]. The IR active modes A_{2u} TO, $3E_u$ TO and A_{2u} LO have peaked at 534.953 cm^{-1} (f_1), 646.460 cm^{-1} (h_1), 724.383 cm^{-1} (j_1) for S_1 and at 523.191 cm^{-1} (f_2), 612.706 cm^{-1} (h_2), 703.099 cm^{-1} (j_2) for S_2 respectively [50]. The peaks i_1 at 690.629 cm^{-1} and i_2 at 664.848 cm^{-1} are due to the symmetric stretching of the Sn-O-Sn bond [51]. The shifting of FTIR peaks towards high energy values in S_1 as compared to S_2 may have resulted from the size effect [52], indicating the smaller size of NFs as compared to T-NFLs [52].

The optical absorption and emission spectra of S_1 and S_2 are shown in Fig. 3(d) and (e) respectively. From the excitonic peak bound absorption spectra, the band gaps of the samples S_1 and S_2 are found to be 3.74 eV and 3.73 eV respectively, as compared to the bulk band gap of 3.60 eV [19]. This reveals the size dependent widening of the band gap as commonly observed in nano-scale materials [53]. Again, the band gap of S_2 is redshifted from S_1, which may be arising due to the confinement effects [53] from the amalgamated nano-flake and nano-rod structures of T-NFLs. The emission spectra shown in Fig. 3(d) and (e) exhibit luminescence, appearing at Gaussian fitted peaks p_1, q_1, r_1, s_1, t_1, u_1, v_1 at 2.70 eV, 2.82 eV, 2.93 eV, 3.06 eV, 3.21 eV, 3.28 eV, 3.42 eV for sample S_1 and peaks p_2, q_2, r_2, s_2, t_2, u_2, v_2 at 2.69 eV, 2.82 eV, 2.93 eV, 3.04 eV, 3.17 eV, 3.28 eV, 3.43 eV for sample S_2. In comparison with the estimated band gap from absorption studies, the luminescence lines appearing at 3.42 eV (v_1) and 3.43 eV (v_2) refer to the radiative $E_{CB} \rightarrow E_{VB}$ (E_{CB} is the conduction band minima and E_{VB} is the valence band

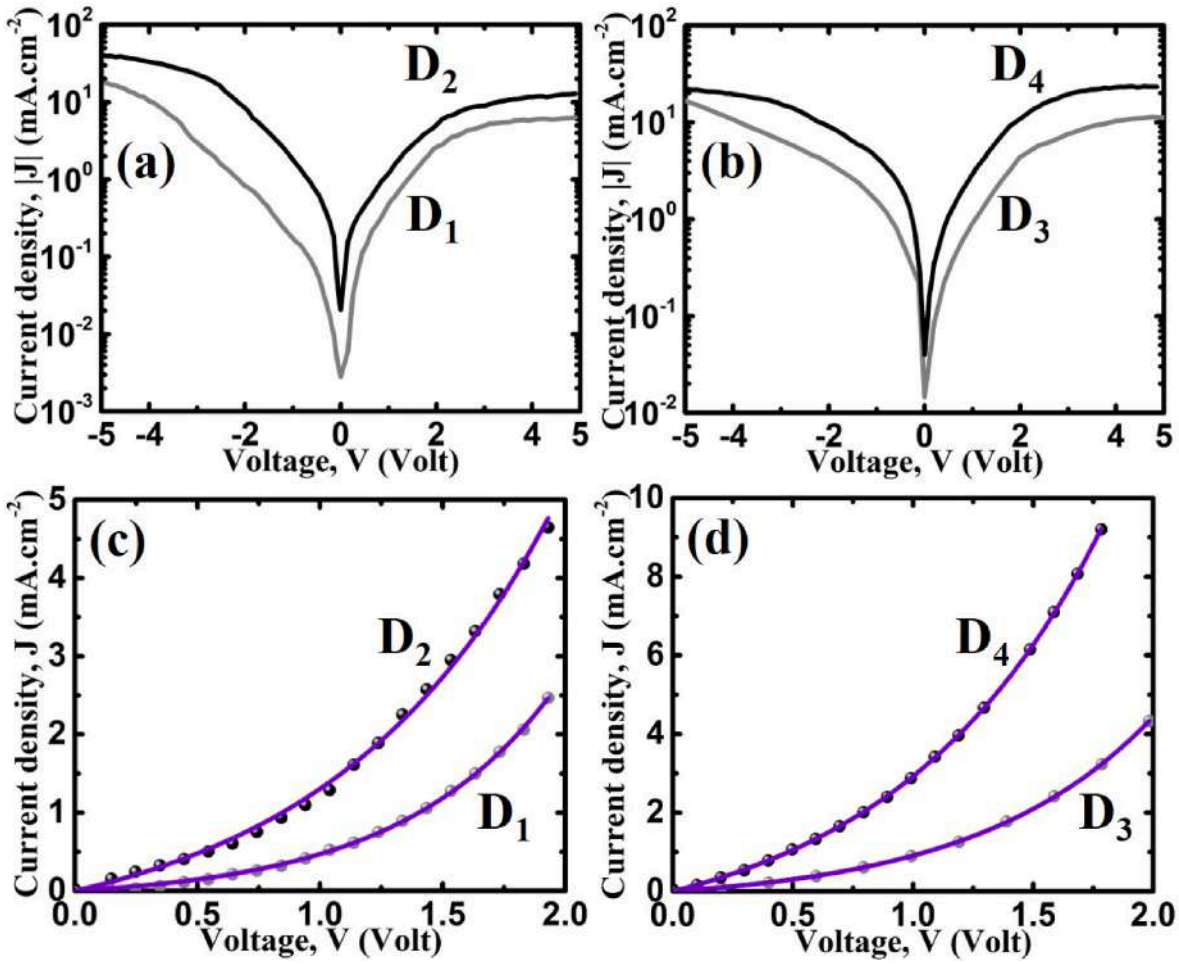

Fig. 5. log(J)~lin(V) curves of (a) D_1 (grey solid line) and D_2 (black solid line), and (b) D_3 (grey solid line) and D_4 (black solid line). (c) and (d) are the forward bias characteristics of D_1 (grey spheres), D_2 (black spheres), and D_3 (grey spheres), D_4 (black spheres) respectively, with fitted curves (violet solid line) using the TE model.

maxima) transition of electrons from the conduction Sn 4p to the valence O 2p band [54]. Further, in case of TCO, the multivalence nature of Sn introduces various intrinsic defect levels within the band gap with fast radiative transitions [55]. The major defect levels originate from interstitial- and vacant- Sn sites and interstitial- and vacant- O sites [55]. Moreover, according to Kilic and Zunger [55] et al., and Fang et al. [56], interstitial Sn^{2+} dominated transitions yield red emission. In our samples, the absence of luminescence at the same level rules out the involvement of Sn interstitial defects mediated transitions. Nevertheless, the origin of the remaining PL peaks can be assigned to the following transitions. In common TCO, there are three types of oxygen vacancies (V_O), *viz.*, neutral oxygen vacancy (V_O^0), singly positively charged oxygen vacancy (V_O^+), and doubly positively charged oxygen vacancy (V_O^{++}) [57]. Notably, at ambient temperature, the dissociation of some V_O^0 gives rise to V_O^+ states and conduction electrons. Now, the V_O^+ state interacts in two possible ways, *viz*, (i) bound to the nearest Sn^{4+} to form a V_O^+ donor level below the conduction band, and (ii) accept a hole to form a V_O^{++} level above (around 1 eV [58]) the valence band. Interestingly, the V_O^{++} form a filled flat energy level above the valence band maxima called V_O^{++} acceptor level and a conduction band resonant empty level called donor level [57,58]. Therefore, the peaks p_1, q_1, r_1, s_1, (t_1 and u_1) and p_2, q_2, r_2, s_2, (t_2 and u_2) may have originated from the radiative transitions, $V_O^+ \rightarrow V_O^{++}$, $V_O^+ \rightarrow E_{VB}$, $V_O^0 \rightarrow V_O^{++}$, $E_{CB} \rightarrow V_O^{++}$ and $V_O^0 \rightarrow E_{VB}$ respectably. Here, the $V_O^0 \rightarrow E_{VB}$ is responsible for two emission peaks (t and u), implying a higher concentration of V_O^0 as compared to that of V_O^+, and V_O^{++} in the samples [59]. The Stoke's shift given by, $\varepsilon_{ab} - \varepsilon_{pl} = 2\delta\varepsilon_{ph}$, where ε_{ab} is the maxima of the absorption band, ε_{pl} is the maxima of the band edge emission, ε_{ph} is the phonon energy (78 meV) [60], and δ is the electron-phonon coupling parameter [61]. Using the values of ε_{ab}, ε_{pl}, and ε_{ph}, the above equation yields the size dependent δ values of 2.09 and 1.94 for S_1 and S_2 respectively. This indicates, the electron-phonon coupling in S_2 has been relaxed due to the size hierarchical nano-trichome structure [62].

The electrical characteristics of the samples were evaluated by fabricating metal-semiconductor junctions comprising semiconductor samples with Au or ITO as the metallic part. The schematic diagram of the device structure is shown in Fig. 4 (a). Notably, the difference in work function between finger electrodes, Ag and samples prevails to be Ohmic contact. From a typical FESEM study of cleaved devices, as shown in Fig. 4 (b), the average thicknesses of the metal and sample layers were estimated as 200 nm and 20 μm respectively. The semi-logarithmic current density-voltage (J-V) plots of the devices D_1 (grey line) and D_2 (black line) shown in Fig. 5(a) and D_3 (grey line) and D_4 (black line) shown in Fig. 5(b) exhibit the typical diode characteristics under dark condition. According to the literature, the work functions of n-type bulk SnO_2, Au, and ITO are ~4.5 eV, ~5.4, and ~5.2 eV respectively [63–65]. Therefore, the SBD characteristics observed in Fig. 5 are consistent with theory. In general, the Schottky behavior is characterized by the thermionic emission (TE) model; $J_D = J_0\left[\exp\left(\frac{qV_D}{\partial k_\beta T}\right) - 1\right]$, where J_D is the current density through the junction, q is the electronic

Table 1
Junction parameters of the fabricated Schottky devices.

Device	J_0 (mA.cm^{-2})	θ	Φ_B (eV)	χ (eV)
D_1	0.140	2.42	0.86	4.52
D_2	0.652	3.52	0.82	4.56
D_3	0.302	2.83	0.84	4.36
D_4	0.141	3.33	0.80	4.40

charge, V_D is the voltage across the junction, θ is the ideality factor, k_β is the Boltzmann constant, T is the absolute temperature, and J_0 is the reverse saturation current [66] where $J_0 = A^{**}T^2 \exp\left(-\frac{q\varphi_B}{k_\beta T}\right)$, with φ_B as the barrier height, and A^{**} as the Richardson constant given by; $A^{**} = 4\pi q m^* k_\beta^2 / h^3$, consists of standard constants [67]. Considering effective mass, m^* as 0.3 m_0 (m_0 is the mass of electron), A^{**} value is 36.06 A cm^{-2}K^{-2} [67] for SnO_2. The J-V curves have been analyzed using the above TE model. The theoretical curves are shown by violet-colored lines in Fig. 5(c). From the best fit, the SBD junction parameters have been extracted and are listed in Table 1. Comparing devices D_1 and D_2, it has been seen that the barrier height of SnO_2 T-NFLs is less than NFs by 0.04 eV, with a difference in the ideality factor as 1.1. Notably, our studies affirm the temperature dependent increment in barrier height, which will be discussed elsewhere. Again, we know that $\varphi_B = \psi_m - \chi_{sc}$ where, ψ_m and χ_{sc} are metal work function and semiconductor electron affinity respectively [68]. Taking ψ_m^{Au} as 5.38 eV [64], the values of χ_{sc} for NFs and T-NFLs are found to be 4.52 eV and 4.56 eV respectively. Similar analysis has been followed for devices D_3 and D_4 that are shown in Fig. 5(d), and the barrier heights are estimated to be 0.84 eV and 0.80 eV respectively with difference in ideality factors by 0.50. Here, the varying barrier heights can be understood as follows. In general, the oxygen vacancies in MO introduce shallow defect layers within the band gap corresponding to V_O^0, V_O^+ and V_O^{++} states. According to the literature, V_O^+ and V_O^{++} states are observed near the conduction band and valence band respectively [57,58]. Therefore, the increase in barrier height in sample S_1 over S_2 may be due to the dominance of V_O^{++} states. Considering the value of $\psi_m^{ITO} = 5.2\ eV$ [65], the χ_{sc} values for both the NFs and T-NFLs are found to be 4.36 eV and 4.40 eV respectively. Further, the barrier heights of devices D_3 and D_4 have lower values compared to D_1 and D_2 respectively. This may be due to the interaction of the metal part's electronic structure and work function with nano-scale semiconductors [69]. The high value of θ indicates rapid tunneling and recombination at the interface of S_2 based devices as compared to S_1 [70]. In comparison with recent reports by B. Jang et al. [68] and S. Jana et al. [71], our samples exhibit improved Schottky barrier height, which is an indicator of better rectification properties [72] (low forward voltage drop and low reverse leakage current). These characteristics render it suitable for a diverse array of applications, encompassing high-speed switching as well as power conversion devices [73].

In order to explore the solar cell performance of the TCO based Schottky junctions, the devices were tested using a solar simulator under 1 sun light excitation. Here, the SBD junctions Au/SnO_2 and ITO/SnO_2 are forwardly biased (positive terminal connected to the bottom metal layer and negative terminal connected to the SnO_2 sample layer having Ohmic Ag finger electrodes) to evaluate the solar cell behavior of the devices. The presence of finger electrodes enables sufficient sunlight transmission through the active layer to reach the junction. Using energy-band diagrams, Fig. 6 schematically explains the origin of the solar energy conversion mechanism. Under forward bias, the electrons move from semiconductor to metal, ensuing the SBD J-V behavior. After photo-excitation, electron-hole pairs were formed across the band edges of the sample sides of the SBD junction. Due to the band bending and decrease in barrier height, the inbuilt electric field at the SBD junction efficiently separates the charge carriers and minimizes the rate of recombination augmenting the energy conversion [74,75]. The J-V characteristics of D_1 and D_2 are shown in Fig. 7(a) and (b) respectively, under illumination conditions. In order to ascertain the solar cell parameters, the data from the 4th quadrant were replotted as insets. From the analysis, the D_1 exhibits short circuit current density, J_{sc} and open circuit voltage, V_{oc} as 0.579 mA cm^{-2} and 0.64 V respectively. Using power maximization protocol, the fill factor (FF) has been estimated to be 60% with solar cell efficiency (η) of 0.22%. Similarly, the J-V analysis of D_2, shown in Fig. 7(b), resulted the Jsc, Voc, FF, and η values as 0.950 mA.cm-2, 0.70 V, 61%, and 0.41%, respectively. Furthermore, the J-V curves of D_3 and D_4 shown in Fig. 8 were analyzed, and the parameters were found to be 1.228 mA cm^{-2} and 2.003 mA cm^{-2} for J_{sc}, 1.33 V and 1.56 V for V_{oc}, 52% and 57% for FF, 0.85% and 1.78% for η respectively. All of the solar cell parameter values for each device are listed in Table 2. The standard deviation in the devices' performance (conversion efficiency) assessed over several batches of samples is found to be 0.03. Again, according to the relation, $V_{oc} = \frac{k_\beta T}{q} \ln\left(\frac{J_{sc}}{J_0} + 1\right)$, where J_0 is the reverse saturation current, the V_{oc} is inversely proportional to J_0 [76]. Hence, the high V_{oc} value observed in our samples is an indicator of low reverse saturation current, implying very negligible recombination of the carriers at the interface [76]. Therefore, the high V_{oc} and excellent filling factor (>50%) observed in our samples suggests feasible power conversion applications [77,78].

4. Conclusion

In conclusion, the alkali ions (K+ and Na+) selective reduction and in-situ crystallization governed by hydrophilic and hydrophobic interactions in a hydrothermal growth yielded tailoring of SnO_2 size from

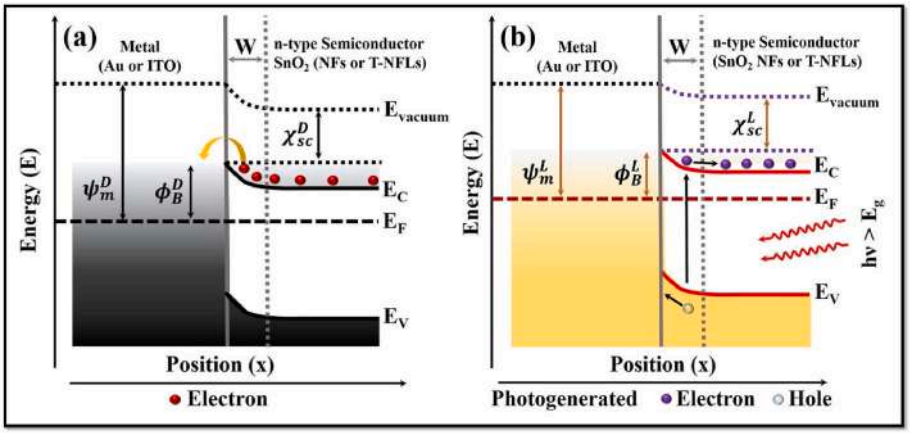

Fig. 6. Energy band diagrams of the devices under (a) dark and (b) 1 sun front illumination conditions.

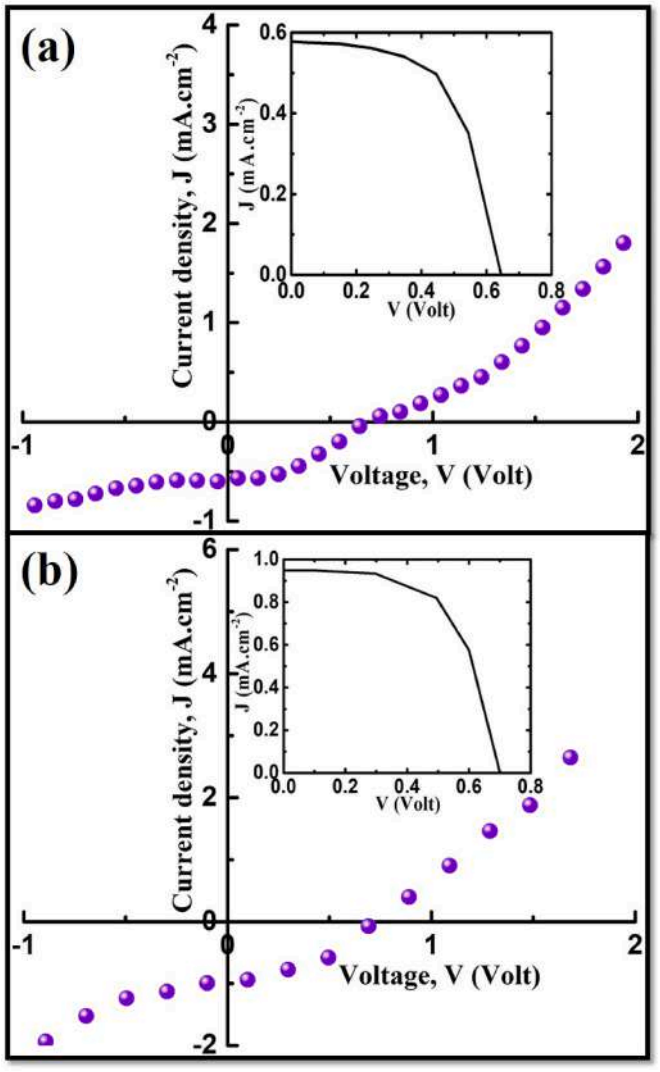

Fig. 7. J ~ V characteristics of D_1 (a) and D_2 (b) under 1 sun illumination, with insets depicting the respective replotted fourth quadrant data.

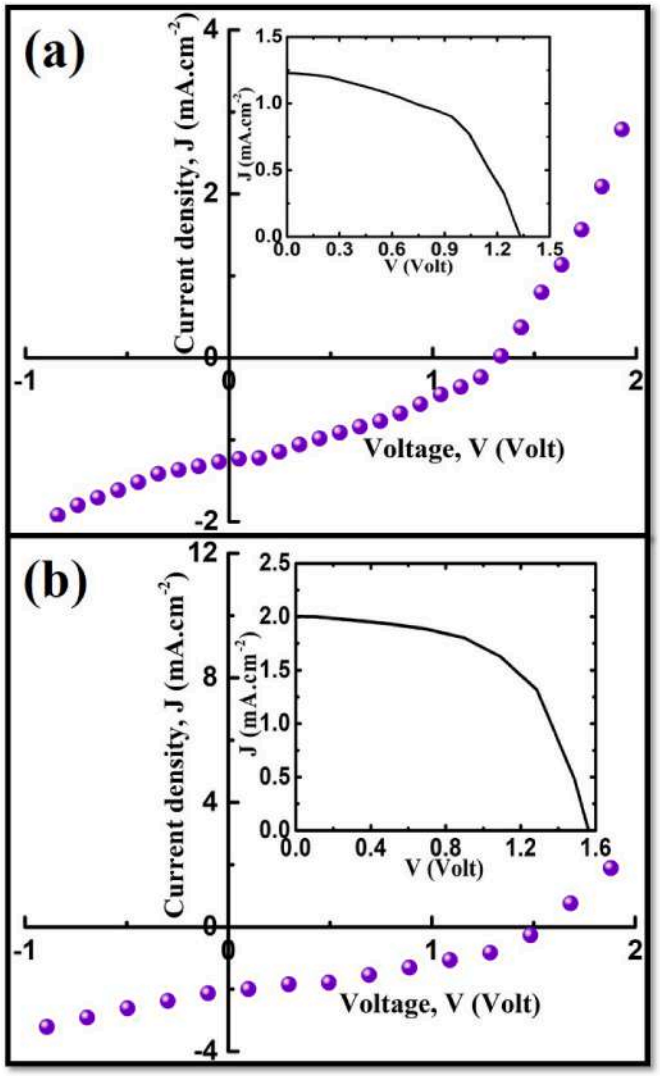

Fig. 8. J ~ V characteristics of D_3 (a) and D_4 (b) under 1 sun illumination, with insets depicting the respective replotted fourth quadrant data.

nano-flakes to trichome nano-flowers. The photoluminescence analysis reveals oxygen defect ridden electronic transition accompanied by decrease in electron-phonon coupling parameter from NFs to T-NFLs. Through Schottky junction analysis, the electrical properties of the samples corroborate solar cell behavior with distinct reverse saturation currents. Compared to SnO_2 NFs, the T-NFLs have a higher photo-conversion efficiency (1.76 ± 0.03%) as well as a higher electron affinity (4.56 eV) and fill factor (61%). The observation of high open-circuit voltage reveals minimal recombination of the carriers at the interface due to its distinct structure. The aforementioned size hierarchical feature makes the SnO_2 nanomaterial suitable for prospective applications in Schottky junction based fast electronic devices and as active electron transport layers in solar cells.

CRediT authorship contribution statement

Gyanadeep Mallik: Writing – original draft, Methodology, Visualization, Conceptualization, Investigation, Data curation, Formal analysis. **Atanu Kabiraj:** Formal analysis. **Pragyan Paramira Dash:** Formal analysis. **Priyanka Kumari:** Formal analysis. **Utkalika Priyadarsini Sahoo:** Resources. **Pratap Kumar Sahoo:** Resources, manuscript review. **Satchidananda Rath:** Validation, Resources, Supervision, Conceptualization, Writing – review & editing, Funding acquisition.

Table 2
Solar cell parameters of the fabricated devices.

Device	J_{sc} (mA.cm^{-2})	V_{oc} (V)	P_{max} (mW)	FF (%)	η (%)
D_1	0.579	0.64	0.222	60	0.22
D_2	0.950	0.70	0.406	61	0.41
D_3	1.228	1.33	0.849	52	0.85
D_4	2.003	1.56	1.775	57	1.78

Declaration of competing interest

The authors declare that they have no known competing financial interests or personal relationships that could have appeared to influence the work reported in this paper.

Data availability

Data will be made available on request.

Acknowledgements

The authors acknowledge Nanomission, DST India scheme SR/NM/NS-68/2016 (G) for the financial support and the central

instrumentation facility (CIF) of IIT Bhubaneswar for the characterization of the samples.

Supplementary Information

The details of structural parameter analysis from the XRD data are available in supporting information.

Appendix A. Supplementary data

Supplementary data to this article can be found online at https://doi.org/10.1016/j.optmat.2023.114306.

References

[1] X. Zhang, H. Yu, W. Tang, X. Wei, L. Gao, M. Hong, Q. Liao, Z. Kang, Z. Zhang, Y. Zhang, All-van-der-Waals barrier-free contacts for high-mobility transistors, Adv. Mater. 34 (2022) 1–10, https://doi.org/10.1002/adma.202109521.

[2] M. Zheng, H. Tang, L. Li, Q. Hu, L. Zhang, H. Xue, H. Pang, Hierarchically nanostructured transition metal oxides for lithium-ion batteries, Adv. Sci. 5 (2018), https://doi.org/10.1002/advs.201700592, 1700592-1–24.

[3] Y. Guo, L. Yu, C.Y. Wang, Z. Lin, X.W. Lou, Hierarchical tubular structures composed of Mn-based mixed metal oxide nanoflakes with enhanced electrochemical properties, Adv. Funct. Mater. 25 (2015) 5184–5189, https://doi.org/10.1002/adfm.201501974.

[4] H. Zhai, D. Fan, Q. Li, Scalable and paint-format colored coatings for passive radiative cooling, Sol. Energy Mater. Sol. Cell. 245 (2022), https://doi.org/10.1016/j.solmat.2022.111853, 111853-1–10.

[5] J. Osvald, L. Hrubčín, B. Zaťko, Schottky barrier height inhomogeneity in 4H-SiC surface barrier detectors, Appl. Surf. Sci. 533 (2020), https://doi.org/10.1016/j.apsusc.2020.147389, 147389-1–5.

[6] A. Baltakesmez, S. Tekmen, B. Güzeldir, Temperature dependent current- and capacitance-voltage characteristics of W/n-Si structures with two-dimensional WS2 and three-dimensional WO3 interfaces deposited by RF sputtering technique, Mater. Sci. Semicond. Process. 118 (2020), https://doi.org/10.1016/j.mssp.2020.105204, 105204-1–16.

[7] A. Baltakesmez, Anomalous photo-sensitivity of AL/CH3 NH3PBI3-XCLX/SI/AL vertical junction diodes; photodiode- and solar cell-like, Res. Rev. Sci. Math. Gece Publish. (2021) 123–143 (Chapter 8).

[8] M.A. Salari, M. Sağlam, A. Baltakesmez, B. Güzeldir, Effect of electron radiation on electrical parameters of Zn/n-Si/Au–Sb and Zn/ZnO/n-Si/Au–Sb diodes, J. Radioanal. Nucl. Chem. 319 (2019) 667–678, https://doi.org/10.1007/s10967-018-06401-9.

[9] A. Baltakesmez, Improved barrier parameters and working stability of Au/p-GO/n-lnP/Au–Ge Schottky barrier diode with GO interlayer showing resistive switching effect, Vacuum 168 (2019), https://doi.org/10.1016/j.vacuum.2019.108825, 108825-1–14.

[10] A. Baltakesmez, A. Taşer, Z. Kudaş, B. Güzeldir, D. Ekinci, M. Sağlam, Barrier height modification of n-InP using a silver nanoparticles loaded graphene oxide as an interlayer in a wide temperature range, J. Electron. Mater. 48 (2019) 3169–3182, https://doi.org/10.1007/s11664-019-07088-8.

[11] A. Baltakesmez, M. Sevim, B. Güzeldir, C. Aykaç, M. Biber, Interface application of NiPt alloy nanoparticles decorated rGO nanocomposite to eliminate of contact problem between metal and inorganic/organic semiconductor, J. Alloys Compd. 867 (2021), https://doi.org/10.1016/j.jallcom.2021.158802, 158802-1–15.

[12] P. Sivakumar, H.S. Akkera, T. Ranjeth Kumar Reddy, G. Srinivas Reddy, N. Kambhala, N. Nanda Kumar Reddy, Influence of Ga doping on structural, optical and electrical properties of transparent conducting SnO2 thin films, Optik 226 (2021), https://doi.org/10.1016/j.ijleo.2020.165859, 165859-1–9.

[13] H. Zhai, D. Fan, Q. Li, Dynamic radiation regulations for thermal comfort, Nano Energy 100 (2022), https://doi.org/10.1016/j.nanoen.2022.107435, 107435-1–32.

[14] M.M. Bagheri Mohagheghi, S. Tabatabai Yazdi, M. Mousavi, Transport, structural and optical properties of SnO2 transparent semiconductor thin films alloyed with chromium: carrier type conversion, J. Mater. Sci. Mater. Electron. 28 (2017) 13328–13335, https://doi.org/10.1007/s10854-017-7169-y.

[15] O. Mounkachi, E. Salmani, M. Lakhal, H. Ez-Zahraouy, M. Hamedoun, M. Benaissa, A. Kara, A. Ennaoui, A. Benyoussef, Band-gap engineering of SnO2, Sol. Energy Mater. Sol. Cell. 148 (2016) 34–38, https://doi.org/10.1016/j.solmat.2015.09.062.

[16] W. Zhou, Y. Liu, Y. Yang, P. Wu, Band gap engineering of SnO2 by epitaxial strain: experimental and theoretical investigations, J. Phys. Chem. C 118 (2014) 6448–6453, https://doi.org/10.1021/jp500546r.

[17] R. Yu, X. Wei, G. Wu, Z. Tan, Layer-by-layered organic solar cells: morphology optimizing strategies and processing techniques, Aggregate 3 (2021) 1–21, https://doi.org/10.1002/agt2.107.

[18] S. Calnan, A.N. Tiwari, High mobility transparent conducting oxides for thin film solar cells, Thin Solid Films 518 (2010) 1839–1849, https://doi.org/10.1016/j.tsf.2009.09.044.

[19] J.H. He, T.H. Wu, C.L. Hsin, K.M. Li, L.J. Chen, Y.L. Chueh, L.J. Chou, Z.L. Wang, Beaklike SnO2 nanorods with strong photoluminescent and field-emission properties, Small 2 (2006) 116–120, https://doi.org/10.1002/smll.200500210.

[20] Q. Jiang, X. Zhang, J. You, SnO2: a wonderful electron transport layer for perovskite solar cells, Small 14 (2018), https://doi.org/10.1002/smll.201801154, 1801154-1–14.

[21] E.R. Viana, J.C. González, G.M. Ribeiro, A.G. De Oliveira, Photoluminescence and high-temperature persistent photoconductivity experiments in SnO2 nanobelts, J. Phys. Chem. C 117 (2013) 7844–7849, https://doi.org/10.1021/jp312191c.

[22] Y.S. Nagaraju, H. Ganesh, S. Veeresh, H. Vijeth, M. Basappa, H. Devendrappa, Self-templated one-step hydrothermal synthesis of hierarchical actinomorphic flower-like SnO2-ZnO nanorods for high-performance supercapacitor application, J. Electroanal. Chem. 900 (2021), https://doi.org/10.1016/j.jelechem.2021.115741, 115741-1–10.

[23] S. Vignesh, G. Palanisamy, M. Srinivasan, N. Elavarasan, K. Bhuvaneswari, G. Venkatesh, T. Pazhanivel, P. Ramasamy, M.A. Manthrammel, M. Shkir, Fabricating SnO2 and Cu2O anchored on g-C3N4 nanocomposites for superior photocatalytic various organic pollutants degradation under simulated sunlight exposure, Diam. Relat. Mater. 120 (2021), https://doi.org/10.1016/j.diamond.2021.108606, 108606-1–12.

[24] A. Baltakesmez, Electrical characterization and solar light sensitivity of SnS2/n-Si junction, J. Inst. of Sci. Technol. 10 (2020) 214–224, https://doi.org/10.21597/jist.642111.

[25] Jun-Jun Xue, Dun-Jun Chen, B. Liu, X.I.E. Zi-Li, Ruo-Lian Jiang, Rong Zhang, Z.H. E.N.G. You-Dou, Au/Pt/inGaN/GaN heterostructure Schottky prototype solar cell, Chin. Phys. Lett. 26 (2009), 098102-1–4.

[26] M. Kim, M.A. Rehman, K.M. Kang, Y. Wang, S. Park, H.S. Lee, S.B. Roy, S.H. Chun, C.A. Singh, S.C. Jun, H.H. Park, The role of oxygen defects engineering via passivation of the Al2O3 interfacial layer for the direct growth of a graphene-silicon Schottky junction solar cell, Appl. Mater. Today 26 (2022), https://doi.org/10.1016/j.apmt.2021.101267, 101267-1–9.

[27] H. Zhai, C. Liu, D. Fan, Q. Li, Dual-encapsulated nanocomposite for efficient thermal buffering in heat-generating radiative cooling, ACS Appl. Mater. Interfaces 14 (2022) 57215–57224, https://doi.org/10.1021/acsami.2c13991.

[28] K. Sato, Y. Yokoyama, J.C. Valmalette, K. Kuruma, H. Abe, T. Takarada, Hydrothermal growth of tailored SnO2 nanocrystals, Cryst. Growth Des. 13 (2013) 1685–1693, https://doi.org/10.1021/cg400013q.

[29] M. Guan, X. Zhao, L. Duan, M. Cao, W. Guo, J. Liu, W. Zhang, Controlled synthesis of SnO2 nanostructures with different morphologies and the influence on photocatalysis properties, J. Appl. Phys. 114 (2013) 2–9, https://doi.org/10.1063/1.4821140.

[30] J. Wang, P. Ma, L. Xiang, Effects of NaOH on formation of ZnO nanorods from ε-Zn(OH)2, Mater. Lett. 141 (2015) 118–121, https://doi.org/10.1016/j.matlet.2014.11.081.

[31] Y. An, D. Yin, L. Song, Y. Chen, K. Gao, Hydrothermal synthesis and characterisation of titanate nanomaterial thin films in mixed aqueous NaOH/KOH, Micro & Nano Lett. 15 (2020) 313–316, https://doi.org/10.1049/mnl.2019.0471.

[32] O. Lupan, L. Chow, G. Chai, H. Heinrich, S. Park, A. Schulte, Growth of tetragonal SnO2 microcubes and their characterization, J. Cryst. Growth 311 (2008) 152–155, https://doi.org/10.1016/j.jcrysgro.2008.10.072.

[33] P.S. Shajira, M.J. Bushiri, B.B. Nair, V.G. Prabhu, Energy band structure investigation of blue and green light emitting Mg doped SnO2 nanostructures synthesized by combustion method, J. Lumin. 145 (2014) 425–429, https://doi.org/10.1016/j.jlumin.2013.07.073.

[34] T.M.K. Thandavan, S.M.A. Gani, C.S. Wong, R.M. Nor, Evaluation of Williamson–Hall strain and stress distribution in ZnO nanowires prepared using aliphatic alcohol, J. Nondestr. Eval. 34 (2015), https://doi.org/10.1007/s10921-015-0286-8, 14-1–9.

[35] A. Amanov, B. Urmanov, T. Amanov, Y.S. Pyun, Strengthening of Ti-6Al-4V alloy by high temperature ultrasonic nanocrystal surface modification technique, Mater. Lett. 196 (2017) 198–201, https://doi.org/10.1016/j.matlet.2017.03.059.

[36] S. Gürakar, T. Serin, Comprehensive structural analysis and electrical properties of (Cu, Al and In)-doped SnO2 thin films, Mater. Sci. Eng. B Solid State Mater. Adv. Technol. 251 (2019), https://doi.org/10.1016/j.mseb.2019.114445, 114445-1–8.

[37] K. Manikandan, S. Dhanuskodi, A.R. Thomas, N. Maheswari, G. Muralidharan, D. Sastikumar, Size-strain distribution analysis of SnO2 nanoparticles and their multifunctional applications as fiber optic gas sensors, supercapacitors and optical limiters, RSC Adv. 6 (2016) 90559–90570, https://doi.org/10.1039/c6ra20503h.

[38] P.C. Dey, R. Das, Impact of silver doping on the crystalline size and intrinsic strain of MPA-capped CdTe nanocrystals: a study by Williamson–Hall method and size–strain plot method, J. Mater. Eng. Perform. 30 (2021) 652–660, https://doi.org/10.1007/s11665-020-05358-9.

[39] X. Mathew, J.P. Enriquez, C. Mejía-García, G. Contreras-Puente, M.A. Cortes-Jacome, J.A. Toledo Antonio, J. Hays, A. Punnoose, Structural modifications of SnO 2 due to the incorporation of Fe into the lattice, J. Appl. Phys. 100 (2006), https://doi.org/10.1063/1.2357635, 073907-1–8.

[40] G. Pradhan, A.K. Sharma, Anomalous Raman and photoluminescence blue shift in mono- and a few layered pulsed laser deposited MoS2 thin films, Mater. Res. Bull. 102 (2018) 406–411, https://doi.org/10.1016/j.materresbull.2018.03.001.

[41] P. Sangeetha, V. Sasirekha, V. Ramakrishnan, Micro-Raman investigation of tin dioxide nanostructured material based on annealing effect, J. Raman Spectrosc. 42 (2011) 1634–1639, https://doi.org/10.1002/jrs.2919.

[42] S.H. Sun, G.W. Meng, G.X. Zhang, T. Gao, B.Y. Geng, L.D. Zhang, J. Zuo, Raman scattering study of rutile SnO2 nanobelts synthesized by thermal evaporation of Sn powders, Chem. Phys. Lett. 376 (2003) 103–107, https://doi.org/10.1016/S0009-2614(03)00965-5.

[43] Q. Liu, H. Zhan, X. Huang, Y. Song, S. He, X. Li, C. Wang, Z. Xie, High visible light photocatalytic activity of SnO2-x nanocrystals with rich oxygen vacancy, Eur. J. Inorg. Chem. 2021 (2021) 4370–4376, https://doi.org/10.1002/ejic.202100617.

[44] L. Abello, B. Bochu, A. Gaskov, S. Koudryavtseva, G. Lucazeau, M. Roumyantseva, Structural characterization of nanocrystalline SnO2 by X-ray and Raman spectroscopy, J. Solid State Chem. 135 (1998) 78–85, https://doi.org/10.1006/jssc.1997.7596.
[45] L. Ying-Kai, D. Yi, W. Guang-Hou, Low-frequency and abnormal Raman spectrum in SnO2 nanorods, Chin. Phys. Lett. 21 (2004) 156–159.
[46] M. Marikkannan, V. Vishnukanthan, A. Vijayshankar, J. Mayandi, J.M. Pearce, A novel synthesis of tin oxide thin films by the sol-gel process for optoelectronic applications, AIP Adv. 5 (2015), https://doi.org/10.1063/1.4909542, 027122-1–8.
[47] D. Amalric-Popescu, F. Bozon-Verduraz, Infrared studies on SnO2 and Pd/SnO2, Catal. Today 70 (2001) 139–154.
[48] R.G. Pavelko, A.A. Vasiliev, E. Llobet, X. Vilanova, N. Barrabés, F. Medina, V. G. Sevastyanov, Comparative study of nanocrystalline SnO2 materials for gas sensor application: thermal stability and catalytic activity, Sensor. Actuator. B Chem. 137 (2009) 637–643, https://doi.org/10.1016/j.snb.2008.12.025.
[49] K.C. Suresh, S. Surendhiran, P. Manoj Kumar, E. Ranjth Kumar, Y.A.S. Khadar, A. Balamurugan, Green synthesis of SnO2 nanoparticles using Delonix elata leaf extract: evaluation of its structural, optical, morphological and photocatalytic properties, SN Appl. Sci. 2 (2020), https://doi.org/10.1007/s42452-020-03534-z, 1735-1–13.
[50] V. Senthilkumar, P. Vickraman, M. Jayachandran, C. Sanjeeviraja, Synthesis and characterization of SnO2 nanopowder prepared by precipitation method, J. Dispersion Sci. Technol. 31 (2010) 1178–1181, https://doi.org/10.1080/01932690903223856.
[51] A. Kumar, L. Rout, R.S. Dhaka, S.L. Samal, P. Dash, Design of a graphene oxide-SnO2 nanocomposite with superior catalytic efficiency for the synthesis of β-enaminones and β-enaminoesters, RSC Adv. 5 (2015) 39193–39204, https://doi.org/10.1039/c5ra03363b.
[52] Y. Wang, A. Muramatsu, T. Sugimoto, FTIR analysis of well-defined α-Fe2O3 particles, Colloids Surf. A Physicochem. Eng. Asp. 134 (1998) 281–297, https://doi.org/10.1016/S0927-7757(97)00102-7.
[53] G. Muthulakshmi, M. Mohamed Ismail, M. Arivanandhan, A. Bhaskaran, Effect of calcination on structural, morphological and electrochemical properties of SnO2 nanoparticles, J. Mater. Sci. Mater. Electron. 33 (2022) 5534–5551, https://doi.org/10.1007/s10854-022-07742-8.
[54] S.H. Luo, Q. Wan, W.L. Liu, M. Zhang, Z.T. Song, C.L. Lin, P.K. Chu, Photoluminescence properties of SnO2 nanowhiskers grown by thermal evaporation, Prog. Solid State Chem. 33 (2005) 287–292, https://doi.org/10.1016/j.progsolidstchem.2005.11.008.
[55] C. Kilic, A. Zunger, Origins of coexistence of conductivity and transparency in SnO2, Phys. Rev. Lett. 88 (2002) 955011–955014, https://doi.org/10.1103/PhysRevLett.88.095501.
[56] M. Fang, X. Tan, B. Cheng, L. Zhang, SnO2 hierarchical nanostructure and its strong narrow-band photoluminescence, J. Mater. Chem. 19 (2009) 1320–1324, https://doi.org/10.1039/b817530f.
[57] R.K. Mishra, A. Kushwaha, P.P. Sahay, Influence of Cu doping on the structural, photoluminescence and formaldehyde sensing properties of SnO2 nanoparticles, RSC Adv. 4 (2014) 3904–3912, https://doi.org/10.1039/c3ra43709d.
[58] N.M.A. Hadia, M.F. Hasaneen, M.A. Hassan, S.H. Mohamed, Effect of the carrier gas on morphological, optical and electrical properties of SnO2 nanostructures prepared by vapor transport, J. Mater. Sci. Mater. Electron. 29 (2018) 4155–4162, https://doi.org/10.1007/s10854-017-8360-x.
[59] D.M. Hofmann, D. Pfisterer, J. Sann, B.K. Meyer, R. Tena-Zaera, V. Munoz-Sanjose, T. Frank, G. Pensl, Properties of the oxygen vacancy in ZnO, Appl. Phys. Mater. Sci. Process 88 (2007) 147–151, https://doi.org/10.1007/s00339-007-3956-2.
[60] E. Burkel, J. Peisl, B. Dorner, Observation of inelastic x-ray scattering from phonons, EPL 3 (1987) 957–961, https://doi.org/10.1209/0295-5075/3/8/015.
[61] M. De Jong, L. Seijo, A. Meijerink, F.T. Rabouw, Resolving the ambiguity in the relation between Stokes shift and Huang-Rhys parameter, Phys. Chem. Chem. Phys. 17 (2015) 16959–16969, https://doi.org/10.1039/c5cp02093j.
[62] Wenyan Liu, Yu Zhang, Weiwei Zhai, Y. Wang, T. Zhang, P. Gu, H. Chu, H. Zhang, T. Cui, Y. Wang, J. Zhao, W.W. Yu, Temperature-dependent photoluminescence of ZnCuInS/ZnSe/ZnS quantum dots, J. Phys. Chem. C 117 (2013) 19288–19294, https://doi.org/10.3788/fgxb20123309.0923.
[63] K. Rachut, C. Körber, J. Brötz, A. Klein, Growth and surface properties of epitaxial SnO2, Phys. Status Solidi A 211 (2014) 1997–2004, https://doi.org/10.1002/pssa.201330367.
[64] M. UdaAb, A. Nakamura, T. Yamamoto Ab, Y. Fujirnoto, Work function of polycrystalline Ag, Au and Al, J. Electron. Spectrosc. Relat. Phenom. 88–91 (1998) 643–648.
[65] J. Rittich, S. Jung, J. Siekmann, M. Wuttig, Indium-Tin-oxide (ITO) work function tailoring by covalently bound carboxylic acid self-assembled monolayers, Phys. Status Solidi B 255 (2018) 27–29, https://doi.org/10.1002/pssb.201800075.
[66] S.K. Cheung, N.W. Cheung, Extraction of Schottky diode parameters from forward current-voltage characteristics, Appl. Phys. Lett. 49 (1986) 85–87, https://doi.org/10.1063/1.97359.
[67] P. Docampo, H.J. Snaith, Obviating the requirement for oxygen in SnO2-based solid-state dye-sensitized solar cells, Nanotechnology 22 (2011), https://doi.org/10.1088/0957-4484/22/22/225403, 225403-1–8.
[68] B. Jang, T. Kim, S. Lee, W.Y. Lee, J. Jang, Schottky nature of Au/SnO2 ultrathin film diode fabricated using sol-gel process, IEEE Electron. Device Lett. 39 (2018) 1732–1735, https://doi.org/10.1109/LED.2018.2871211.
[69] Z. Caldiran, Modification of Schottky barrier height using an inorganic compound interface layer for various contact metals in the metal/p-Si device structure, J. Alloys Compd. 865 (2021), https://doi.org/10.1016/j.jallcom.2021.158856, 158856-1–13.
[70] S. Rajaputra, S. Vallurupalli, V.P. Singh, Copper phthalocyanine based Schottky diode solar cells, J. Mater. Sci. Mater. Electron. 18 (2007) 1147–1150, https://doi.org/10.1007/s10854-007-9152-5.
[71] S. Jana, S. Pramanik, B. Show, A. Mondal, S. Mukhopadhyay, A new strategy to fabricate SnS-SnO2 heterostructure with excellent photoresponse and charge transport properties: efficient photocatalyst for fast photoreduction of Cr(VI), Mater. Sci. Eng. B: Solid State Mater. Adv. Technol. 275 (2022), https://doi.org/10.1016/j.mseb.2021.115520, 115520-115521–9.
[72] K.J. Schoen, J.M. Woodall, J.A. Cooper, M.R. Melloch, Design considerations and experimental analysis of high-voltage SiC Schottky barrier rectifiers, IEEE Trans. Electron. Dev. 45 (1998) 1595–1604, https://doi.org/10.1109/16.701494.
[73] Q. Yan, X. Yuan, Y. Geng, A. Charalambous, X. Wu, Performance evaluation of split output converters with SiC MOSFETs and SiC Schottky diodes, IEEE Trans. Power Electron. 32 (2017) 406–422, https://doi.org/10.1109/TPEL.2016.2536643.
[74] Q. Zhang, Q. Liang, D.K. Nandakumar, S.K. Ravi, H. Qu, L. Suresh, X. Zhang, Y. Zhang, L. Yang, A.T.S. Wee, S.C. Tan, Energy harvesting from shadow-effect, Energy Environ. Sci. 13 (2020) 2404–2413, https://doi.org/10.1039/d0ee00825g.
[75] A.K. Jehad, M. Yurddaskal, F. Gunes, C. Zafer, K. Kocabas, Investigation of graphene-based Schottky junction solar cell with heavy-doped silicon, J. Mater. Sci. Mater. Electron. 32 (2021) 28856–28869, https://doi.org/10.1007/s10854-021-07270-x.
[76] R. Brendel, H.J. Queisser, On the thickness dependence of open circuit voltages of p-n junction solar cells, Sol. Energy Mater. Sol. Cell. 29 (1993) 397–401, https://doi.org/10.1016/0927-0248(93)90098-N.
[77] Z. Guo, A.K. Jena, G.M. Kim, T. Miyasaka, The high open-circuit voltage of perovskite solar cells: a review, Energy Environ. Sci. 15 (2022) 3171–3222, https://doi.org/10.1039/d2ee00663d.
[78] D. Liu, Y. Wang, H. Xu, H. Zheng, T. Zhang, P. Zhang, F. Wang, J. Wu, Z. Wang, Z. Chen, S. Li, SnO2-Based perovskite solar cells: configuration design and performance improvement, Sol. RRL 3 (2019), https://doi.org/10.1002/solr.201800292, 1800292-1–22.